

A new hypothesis for bimodal volcanism in the Kermadec Arc

Yasuhiro Hirai, * a, b, (1) Yoshihiko Tamura^b

^a *Division of Natural System, Kanazawa University, 920-1192 Ishikawa, Japan*

^b *Research Institute for Marine Geodynamics, Japan Agency for Marine-Earth Science and Technology (JAMSTEC), 237-0061 Kanagawa, Japan*

*Corresponding author ([deep.forest.alliance \[at\] gmail.com](mailto:deep.forest.alliance[at]gmail.com))

Abstract

Bimodal volcanism of basaltic and rhyolitic magmas in the Kermadec Arc has been attributed to the fractional crystallization of basaltic sources. However, new evidence from the Kibblewhite Volcano reveals two distinct differentiation pathways originating from mantle-derived basaltic and andesitic primary magmas. Here we employ geothermobarometric estimations, mass-balance calculations, and thermodynamic modeling to demonstrate that rhyolitic magmas in the Kibblewhite Volcano are derived from andesitic primary magmas through ~70% fractional crystallization. The andesite differentiation model provides a more efficient pathway for rhyolite generation than the basalt differentiation model, supported by rare earth element compositions and differentiation modelling. We propose a new hypothesis that bimodal volcanism in the Kermadec Arc arises from parallel differentiation of basaltic and andesitic primary magmas, a process facilitated by the thin crust in this arc and varied mantle melting conditions. This study challenges conventional basalt-centric paradigms of silicic magma genesis and highlights the importance of mantle-derived andesitic magmas in shaping oceanic arc volcanism.

Introduction

Submarine volcanoes frequently produce explosive eruptions that significantly impact Earth's surface. For instance, the 2012 Havre Volcano eruption in Tonga Arc¹⁻³ and the 2021 Fukutoku-Oka-no-Ba eruption in Ogasawara Arc^{4,5} created extensive pumice rafts, disrupting the ecology and economy of the Western Pacific. Similarly, the 2022 Hunga Tonga-Hunga Ha'apai eruption generated tsunamis observed worldwide⁶. These events underscore the importance of understanding the origin of silicic magmas in oceanic arcs for both geological research and disaster mitigation.

The Kermadec Arc, an active oceanic arc in the Western Pacific, is characterized by a thin crust (<15 km)⁷ and bimodal volcanism involving basaltic (50-57 wt.% SiO₂

with total volume ~1500 km³) and rhyolitic (63–73 wt.% SiO₂ with total volume ~900 km³) magmas^{8,9}. While the origin of silicic magmas in the Kermadec Arc has been debated, consensus suggests they are derived from basaltic sources. Early studies^{8,10–12} proposed that lower crustal amphibolite melting could generate silicic magmas; however, recent research favors a model where 70–80% fractional crystallization of basaltic melt produces dacitic to rhyolitic magmas^{13–16}. This preference arises because (1) the oxygen isotope compositions of dacites and rhyolites more closely match mantle-derived melts^{14,17} and (2) amphibolite melting does not adequately explain the rare earth element (REE) concentrations in silicic magmas^{14,18}. However, magma erupting through a thin crust is less likely to be heavily influenced by fractional crystallization or crustal contributions due to its shorter ascent path. Thus, the origin of the voluminous rhyolitic magmas in the Kermadec Arc remains a challenge.

Recently study by Hirai et al.¹⁹ identified magnesian andesites at the Kibblewhite Volcano and estimated their primary melt compositions, referred to as Kibblewhite high-magnesian andesites (HMAs). These melts are believed to be mantle-derived andesitic magmas generated under low-pressure conditions in the upper mantle. Additionally, Hirai et al.²⁰ reported olivine-hosted primitive basaltic melt inclusions (PBMI) from the same volcano, representing deeper mantle-derived magmas predating the magnesian andesites. These findings suggest that the thin crust of the Kermadec Arc facilitates the coexistence of both basaltic and andesitic primary magmas, even within a single volcanic system. Consequently, focusing solely on basaltic sources may be insufficient when explaining the origin of rhyolitic magmas in this arc.

This study aims to elucidate how primary basaltic and andesitic magmas contribute to the formation of rhyolitic magmas in the Kermadec Arc. To achieve this, we first investigate the rhyolitic magma of the Kibblewhite Volcano by estimating magmatic conditions using multiple geothermobarometers and conducting mass balance and thermodynamic fractional crystallization modeling. The results reveal a parent-daughter relationship between the magnesian andesites and rhyolitic magmas in the Kibblewhite Volcano. Finally, we propose a new hypothesis to explain bimodal volcanism in the Kermadec Arc, based on insights derived from the Kibblewhite Volcano.

Background

Kibblewhite Volcano is situated in the southern segment of the Kermadec Arc at approximately 34.6°S and 179.2°E (Fig. S1). Volcanic rocks collected from the area around Kibblewhite Volcano have been classified into several magmatic types based on petrographic and geochemical analyses¹⁹ (Fig.1). The basalts contain olivine ± clinopyroxene + plagioclase phenocrysts, and those that are particularly abundant in olivine and clinopyroxene are called ankaramites. These basaltic samples predominantly

occur in small volcanic cones surrounding the Kibblewhite Volcano (KI1–KI4; Fig. S1). Magnesian andesites include olivine (Fo_{83–86}) and clinopyroxene (Mg# = 82–87) microphenocrysts, with minor forsteritic olivine xenocrysts (Fo_{90–92}). Low-Mg andesites included clinopyroxene (Mg# = 68–75), orthopyroxene (Mg# = 61–74), plagioclase (An_{45–85}), and magnetite ± ilmenite. Dacites and rhyolites are pumiceous rocks with clinopyroxene (Mg# = 64–76), orthopyroxene (Mg# = 55–71), amphibole (Mg# = 54–67), plagioclase (An_{29–60}), and magnetite ± ilmenite. Kibblewhite HMAs, which were calculated by adding 12% olivine (olivine model) or 15% olivine and 6% clinopyroxene (olivine + clinopyroxene model) to magnesian andesite compositions, represent primary andesitic endmembers¹⁹. The olivine-hosted PBMI from the ankaramites and magnesian andesites have major and trace element compositions similar to the ankaramite whole-rock compositions, representing the primary basaltic melts occurring in the Kibblewhite mantle²⁰.

In summary, Kibblewhite Volcano hosts two distinct primary magmas and two types of andesites with contrasting petrological characteristics. These findings support the development of two differentiation models for the generation of rhyolitic magma at the volcano. In the basalt differentiation model, primary basaltic magma evolves into low-Mg andesite (blue arrows in Fig. 1), while in the HMA differentiation model, primary andesitic magma evolves into magnesian andesite (red arrows in Fig. 1). A central question is which differentiation pathway more plausibly accounts for the origin of dacitic and rhyolitic magmas. Both low-Mg and magnesian andesites display Sr-Nd-Hf-Pb isotopic ratios consistent with those of dacites and rhyolites (Fig. S2), indicating that either model could theoretically produce the observed silicic magmas. To resolve this uncertainty, this study examines the magmatic conditions and applies fractional crystallization modeling to determine whether the rhyolitic magmas were derived from low-Mg andesite or magnesian andesite.

Methods

The chemical compositions of all mineral phases in volcanic rocks from the Kibblewhite Volcano were reported by Hira et al.¹⁹, enabling us to estimate the magmatic conditions of these magmas. Based on the observed mineralogy, pre-eruptive magmatic temperatures were determined using the following geothermometer: (1) olivine-melt geothermometer²¹, (2) clinopyroxene geothermometer²² (applicable to basaltic and andesitic samples only), (3) paired clinopyroxene-orthopyroxene geothermometer²³, (4) coexisting ilmenite-magnetite geothermometer²⁴, and (5) amphibole thermometer²⁵. Since geothermometers (1) and (2) are dependent on H₂O content of the melt, we integrated these with a plagioclase-melt hygrometer²⁶ to simultaneously estimate temperature and water content. For amphibole-bearing samples, water contents were further refined using an amphibole hygrometer²⁷. Pressure

conditions were obtained using clinopyroxene barometer²² (for basaltic and andesitic samples) and Al-in-hornblende barometer²⁸. Oxygen fugacity (fO_2) was calculated using a solution model for coexisting magnetite and ilmenite²⁹ and magnetite-melt oxybarometer³⁰. The estimated magmatic conditions are summarized in Table S1.

The basalt and HMA differentiation models were evaluated using least-squares mass balance calculations based on the actual compositions of melt and phenocryst phases (Table S2). The calculations were conducted using OPTIMASBA Microsoft® Excel© spreadsheet³¹ with chemical compositions for parent magmas, daughter magmas, and fractionated phases derived from literature data¹⁹. The fraction of residual melt, along with the mineral assemblages and their proportions among the fractionated minerals, is summarized in Table S3. The calculation of REE concentration in the modeled daughter magmas was performed using the proportions of fractionating phenocryst phases and crystal–liquid partition coefficients, in accordance with the Rayleigh fractionation model. Partition coefficients for REEs were taken from Ewart et al.³² for olivine, clinopyroxene, and orthopyroxene; Nandedkar et al.³³ for amphibole; and Nielsen et al.³⁴ for magnetite.

Thermodynamic fractional crystallization calculations were performed using Rhyolite-MELTS³⁵ (ver. 1.2) and COMAGMAT³⁶ (ver. 3.75). The initial melt compositions, derived from the Kibblewhite HMAs and PBMI, are summarized in Table S4. Given the broad range of CaO/Al₂O₃ ratios observed in PBMI²⁰, two representative compositions with ratios of 0.85 and 1.11 were selected for modeling. The initial melts were assumed to contain 1.0 wt.% and 3.0 wt.% H₂O and were crystallized under isobaric conditions at pressures of 3.0 kbar and 5.0 kbar, with oxidation states set to QFM and $\Delta QFM + 1$. These conditions were chosen based on magmatic parameters estimated from geothermobarometric data for the Kibblewhite magmas.

Results

Magmatic conditions

Figure 2 presents the estimated magmatic conditions (temperature, water content, pressure, and oxygen fugacity) derived from multiple geothermobarometers. The geothermometers indicate that magnesian andesites display temperatures comparable to basalts (1050–1150°C), whereas low-Mg andesites exhibit similar temperatures to dacites and rhyolites (800–900°C). Geohygrometers estimate water contents of 2–4 wt.% for basalts and 5–7 wt.% H₂O for low-Mg andesites, dacites, and rhyolites. Geobarometers distinguish pressure conditions among magnesian andesites (~4 kbar), low-Mg andesites (~1–2 kbar), and dacites and rhyolites (~2–3 kbar).

Oxybarometers estimate oxygen fugacity values for low-Mg andesites (QFM +0.1 to QFM +0.7), which overlap with those of dacites and rhyolites (QFM +0.2 to QFM +1.4). These magmatic conditions for rhyolites align with those of other rhyolites in the Kermadec Arc, such as those from Raoul, Healy, and Macauley¹⁴, and the 2012 Havre Volcano eruption¹⁶.

These estimates suggest that the magnesian andesites have high-temperature and high-pressure conditions akin to basalts, distinctly differing from low-Mg andesites. While geohygrometers are not directly applicable to magnesian andesites, their water contents (1.3-4.8 wt.%) were estimated based on analysis of melt inclusions in olivine xenocrysts²⁰, further distinguishing them from low-Mg andesites (Fig. 2). Importantly, low-Mg andesites show similar temperatures and water contents to dacites and rhyolites but occur at low pressures. This indicates that dacitic and rhyolitic magmas are unlikely to form through the crystallization differentiation of low-Mg andesites.

Mass balance model

The mass balance calculations indicate that both the HMA and basalt differentiation models successfully reproduce the major element compositions of dacites and rhyolites with a low residual sum of squares (Table S2). To further evaluate the parent-daughter relationships, we calculated the REE concentrations of the modeled daughters. Figure 3 shows the REE concentrations for the low-Mg andesite–dacite, magnesian andesite–dacite, and dacite–rhyolite intervals. The results revealed that the major elements of dacite could be reproduced after ~44% fractional crystallization of low-Mg andesite, but its REE concentrations did not match (Fig. 3A). In contrast, both the major and REE compositions of dacite were accurately reproduced after ~39% fractional crystallization of magnesian andesites (Fig. 3B), while the major and REE compositions of rhyolite were reproduced after ~25% fractional crystallization of dacites (Fig. 3C). These findings suggest that dacites and rhyolites are more plausibly formed by fractional crystallization of magnesian andesites rather than low-Mg andesites, particularly in terms of REE concentrations.

Moreover, least-squares mass-balance calculations demonstrated that the primary andesite differentiation model is significantly more efficient in generating silicic magmas than the basalt differentiation model. The HMA differentiation model yielded 46% rhyolitic melts, whereas the basalt differentiation model required more extensive crystal fractionation, producing only 13% rhyolitic melt (Table S3).

Thermodynamic model

Thermodynamic fractional crystallization calculations were conducted using Rhyolite-MELTS³⁵ and COMAGMAT³⁶, employing initial compositions derived from

the Kibblewhite HMAs and PBMI. Figure 4 illustrates the representative compositional evolution of the calculated liquids during 70% crystal fractionation, modeled under specific conditions (initial 3.0 wt.% H₂O, 3.0 kbar, Δ QFM +1). MELTS calculations produced liquids with significantly lower FeO*/MgO, TiO₂, and FeO* values compared to observed trends in the Kibblewhite magmas, which can be attributed to the premature crystallization of Fe-Ti oxides. To address this, the COMAGMAT model was used with corrected liquidus temperatures for Fe-Ti oxides, resulting in compositional trends more consistent with the magmatic variations observed in the Kibblewhite Volcano. However, this modeling does not aim to fully reproduce differentiation trends or evaluate magmatic conditions comprehensively, as the crystallization of Fe-Ti oxides involves complex, interdependent physical properties.

Rather, the most notable distinction between the HMA and PBMI differentiation models lies in the SiO₂ content of the resulting liquids. After 70% crystal fractionation, Kibblewhite HMAs produced rhyolitic liquids, whereas PBMI yielded only andesitic liquids (Fig.4). Although variations in modeling conditions (pressure, water content, and oxygen fugacity) caused slight differences in differentiation pathways, the SiO₂ contents of the final liquids in the HMA differentiation model (65–72 wt.% SiO₂) consistently remained higher than those in the basalt differentiation model (50–63 wt.% SiO₂) (Fig.S3). These findings suggest that PBMI cannot produce rhyolitic melts through a reasonable degree of crystallization (~70%), but the HMAs can.

Discussion

Origin of rhyolitic magmas in the Kibblewhite Volcano

This study evaluates which model—the basalt differentiation model that produces low-Mg andesite or the HMA differentiation model that produces magnesian andesite—is more plausible for the generation of rhyolitic magma at Kibblewhite Volcano. Geothermobarometric analyses reveal that low-Mg andesites exhibit temperatures as low as those of dacites and rhyolites (830–950°C) and contain similarly high-water contents (5.0–6.5 wt.%), indicating that low-Mg andesites are already significantly evolved. Furthermore, mass balance calculations demonstrate that low-Mg andesites cannot account for the REE compositions of dacites and rhyolites, reinforcing the conclusion that low-Mg andesites are unlikely to produce silicic magmas through further fractional crystallization. In contrast, magnesian andesites successfully reproduce both the major and REE compositions of dacites and rhyolites, suggesting that fractional crystallization of magnesian andesites provides a more plausible pathway for the generation of rhyolitic magmas in the Kibblewhite Volcano.

The HMA differentiation model demonstrates a clear advantage in producing silicic magmas more efficiently compared to the basalt differentiation model. Mass balance and thermodynamic models show that ~70% fractional crystallization of Kibblewhite HMAs generates rhyolitic melts, whereas the same degree of crystallization in primitive basaltic melts produces only andesitic compositions. This difference arises from the mineralogy of the fractionated phases (olivine, clinopyroxene, plagioclase), which typically contain ~50 wt.% SiO₂. When basaltic magmas with ~50 wt.% SiO₂ fractionate these minerals, the SiO₂ content of the residual melt remains relatively unchanged. In contrast, andesitic magmas (>55 wt.% SiO₂) enriched in silica can generate rhyolitic melts as fractionation progresses (see Figure 11 in Kelemen et al.³⁷).

In previous studies, 70–80% fractional crystallization of basaltic magmas was proposed to generate rhyolitic compositions in the Kermadec Arc^{13–15,38}. However, this study identifies a key discrepancy arising from differences in the initial melt compositions used in the models. The parental basalts in earlier research were not primitive, with MgO contents of 5.4–7.5 wt.% and FeO*/MgO ratios of 1.2–2.2, indicating that they had already undergone significant differentiation from primary melts. As a result, these studies may have overestimated the final volume of rhyolitic melts produced.

Thus, it is reasonable to conclude that the silicic magmas of the Kibblewhite Volcano were primarily generated through the fractional crystallization of primary andesitic magmas. At the same time, fractional crystallization of primary basaltic magmas likely occurred in parallel, producing low-Mg andesites. Thermodynamic modeling demonstrates that if primary basaltic and andesitic magmas undergo a similar degree of fractional crystallization (~70%), the former produces andesitic magmas with low-temperatures and high-water contents, whereas the latter generates rhyolitic magmas (Fig.4). This finding strongly supports the interpretation that low-Mg andesites were derived from primary basaltic magmas through fractional crystallization. These results highlight the complementary roles of basaltic and andesitic primary magmas in shaping the magmatic diversity of the Kibblewhite Volcano.

New hypothesis for bimodal volcanism in the Kermadec Arc

This study reveals that two types of primary magmas—basaltic and andesitic—formed distinct differentiation trends at the Kibblewhite Volcano, providing a novel mechanism for understanding bimodal volcanism in the Kermadec Arc. As shown in Figure 5, the SiO₂ histogram of magmatic ejecta from the arc displays peaks at 50–57 wt.% and 65–73 wt.% SiO₂, corresponding to 50–70% parallel differentiation of mantle-derived basalt and andesite. In regions with a thin crust, such as the Kermadec Arc, primary magmas can vary from basaltic to andesitic due to mantle melting at

varying pressures^{19,20,39}. These findings suggest that rhyolitic magmas in the Kermadec Arc likely derived from primary andesitic magmas, emphasizing the importance of parallel differentiation processes in bimodal volcanism.

Building on these observations, we propose that the basalt and andesite differentiation series can be effectively distinguished using the FeO*/MgO–SiO₂ diagram. While the Miyashiro⁴⁰ discrimination diagram has been traditionally used to identify differentiation trends, it is inadequate for distinguishing between basaltic and andesitic primary magmas, as shown in Figure 6A. Differentiation trends of primary magmas from the Western Epi in the Vanuatu Arc⁴¹, Monowai in the Kermadec Arc⁴² and Chichijima in the Ogasawara Islands⁴³ demonstrate that the FeO*/MgO values of andesitic series cross the traditional "Miyashiro" discrimination line, challenging its applicability. This limitation arises because Miyashiro's discrimination assumes only basaltic primary magmas occur in volcanic arcs, a premise inconsistent with arcs where both basaltic and andesitic primary melts are present.

To address this, we adopted a new discrimination line based on trends observed in the Ogasawara boninites (broken line in Fig. 6A). Applying this new discrimination to the Kibblewhite Volcano (Fig. 6B), ankaramites, basalts, and low-Mg andesites align with the "basalt differentiation series," while magnesian andesites, dacites, and rhyolites belong to the "andesite differentiation series," consistent with the petrological conclusions of this study. Extending this analysis to the entire Kermadec Arc (Fig. 6C), the FeO*/MgO–SiO₂ variation in dacites and rhyolites resembles trends observed in boninites, further supporting the coexistence of basaltic and andesitic primary magmas across the arc.

Figure 6D compares the application of this discrimination to the Izu Arc, another oceanic arc characterized by bimodal volcanism of basaltic and rhyolitic magmas⁴⁴. Similar FeO*/MgO–SiO₂ variations in the Izu and Kermadec Arcs suggest that rhyolitic magmas in both arcs may have been derived from analogous sources. However, the generation mechanisms for rhyolitic magmas differ between the two arcs. In the Izu Arc, rhyolitic magmas are attributed to dehydration melting of the andesitic middle crust, as evidenced by reversely zoned orthopyroxene phenocrysts^{45,46}. In contrast, dacites and rhyolites in the Kermadec Arc exhibit fewer disequilibrium structures in minerals^{13,14,19}, indicating their formation via fractional crystallization rather than crustal anatexis. Dehydration melting experiments^{45,47} using an andesitic starting material similar to Kibblewhite magnesian andesites yielded liquids consistent with rhyolitic magmas in both arcs (Fig. 6D). This suggests that silicic magmas in both arcs share a common magnesian andesitic source, despite differences in their formation mechanisms.

Based on these findings, we propose a new hypothesis that bimodal volcanism in the Kermadec Arc results from the parallel differentiation of mantle-derived basaltic

and andesitic magmas. This differentiation process, distinguished by $\text{FeO}^*/\text{MgO}-\text{SiO}_2$ trends, offers a fresh perspective on silicic magma genesis in oceanic arcs and highlights the critical role of mantle-derived andesitic magmas in shaping bimodal volcanic systems.

Implications for silicic magma generation in oceanic arcs

To evaluate the applicability of this framework to other oceanic arcs characterized by thin crust, the discrimination line was applied to data from the Tonga Arc (Fig. 6E) and the South Sandwich Arc (Fig. 6F). In both arcs, volcanic activity is predominantly basaltic to andesitic (50–60 wt.% SiO_2) rather than bimodal, with most samples falling within the basalt differentiation series. However, in the Tonga Arc, dacites and rhyolites classified into the andesite differentiation series have been identified in the northern region^{48,49}, suggesting a genetic relationship to nearby boninite samples. Similarly, in the South Sandwich Arc, rhyolites from Protector Shoal are classified into the andesite differentiation series, and andesites from the back-arc volcano Loskov exhibit compositions resembling Kibblewhite magnesian andesites. Although this suggests a potential genetic link, the highly-porphyritic nature and presence of xenocrysts in Loskov andesites⁵⁰ render them unsuitable as parental magmas, leaving the true source of Protector Shoal silicic magmas unresolved. These findings highlight the importance of integrating petrographic analyses into magmatic differentiation studies.

In any case, this framework suggests that silicic magmas in these arcs, like those in the Kermadec Arc, may involve contributions from primary andesitic magmas. However, the scarcity of silicic magmas in these arcs compared to the Kermadec Arc still remains unclear. One possibility is sampling limitation due to erupted materials residing on the seafloor. Primitive magmas may bypass main magma chambers and erupt near the base of volcanic edifices⁵¹.

Conclusion

This study hypothesized that bimodal volcanism in the Kermadec Arc stems from the parallel differentiation of mantle-derived basaltic and andesitic magmas. Basaltic magmas evolve into low-Mg andesites through ~70% fractional crystallization, while andesitic magmas efficiently generate dacites and rhyolites. The application of a new discrimination line based on $\text{FeO}^*/\text{MgO}-\text{SiO}_2$ trends provided a tool for distinguishing basaltic and andesitic differentiation series, revealing systematic variations in magmatic processes. This approach enhances our understanding of the dual roles of primary basaltic and andesitic magmas in shaping the magmatic diversity of oceanic arcs.

Acknowledgements

This work was supported by JSPS KAKENHI Grant Nos. 19J10691 and 24H02520 to Y. H. and Grant No. JP21H01195 to Y. T. Part of this research was supported by the Environment Research and Technology Development Fund (Grant No. JPMEERF20244M02) of the Environmental Restoration and Conservation Agency, provided by the Ministry of the Environment of Japan. We would like to thank Editage (www.editage.jp) for the English language editing.

References

1. Jutzeler, M. *et al.* On the fate of pumice rafts formed during the 2012 Havre submarine eruption. *Nat Commun* 1–10 (2014) doi:10.1038/ncomms4660.
2. Carey, R. J., Wysoczanski, R., Wunderman, R. & Jutzeler, M. Discovery of the Largest Historic Silicic Submarine Eruption. *Eos, Transactions American Geophysical Union* **95**, 157–159 (2014).
3. Velasquez, E. *et al.* Age and area predict patterns of species richness in pumice rafts contingent on oceanic climatic zone encountered. *Ecol Evol* **8**, 5034–5046 (2018).
4. Yoshida, K. *et al.* Variety of the drift pumice clasts from the 2021 Fukutoku-Oka-no-Ba eruption, Japan. *Island Arc* **31**, e12441 (2022).
5. Yoshida, K. *et al.* Oxidation-induced nanolite crystallization triggered the 2021 eruption of Fukutoku-Oka-no-Ba, Japan. *Sci Rep* **13**, 7117 (2023).
6. Lynett, P. *et al.* Diverse tsunamigenesis triggered by the Hunga Tonga-Hunga Ha’apai eruption. *Nature* **609**, 728–733 (2022).
7. Bassett, D. *et al.* Crustal structure of the Kermadec arc from MANGO seismic refraction profiles. *J Geophys Res Solid Earth* **121**, 7514–7546 (2016).
8. Smith, I. E. M., Worthington, T. J., Stewart, R. B., Price, R. C. & Gamble, J. A. Felsic volcanism in the Kermadec arc, SW Pacific: crustal recycling in an oceanic setting. *Geological Society, London, Special Publications* **219**, 99–118 (2003).
9. Wright, I. C., Worthington, T. J. & Gamble, J. A. New multibeam mapping and geochemistry of the 30°–35° S sector, and overview, of southern Kermadec arc volcanism. *Journal of Volcanology and Geothermal Research* **149**, 263–296 (2006).
10. Smith, I. E. M., Stewart, R. B. & Price, R. C. The petrology of a large intra-oceanic silicic eruption: The Sandy Bay Tephra, Kermadec Arc, Southwest Pacific. *Journal of Volcanology and Geothermal Research* **124**, 173–194 (2003).

11. Smith, I. E. M. & Price, R. C. The Tonga-Kermadec arc and Havre-Lau back-arc system: Their role in the development of tectonic and magmatic models for the western Pacific. *Journal of Volcanology and Geothermal Research* **156**, 315–331 (2006).
12. Smith, I. E. M., Stewart, R. B., Price, R. C. & Worthington, T. J. Are arc-type rocks the products of magma crystallisation? Observations from a simple oceanic arc volcano: Raoul Island, Kermadec Arc, SW Pacific. *Journal of Volcanology and Geothermal Research* **190**, 219–234 (2010).
13. Haase, K. M., Stroncik, N., Garbe-Schönberg, D. & Stoffers, P. Formation of island arc dacite magmas by extreme crystal fractionation: An example from Brothers Seamount, Kermadec island arc (SW Pacific). *Journal of Volcanology and Geothermal Research* **152**, 316–330 (2006).
14. Barker, S. J. *et al.* Geochemistry and petrogenesis of silicic magmas in the intra-oceanic Kermadec arc. *Journal of Petrology* **54**, 351–391 (2013).
15. Keith, M. *et al.* Constraints on the source of Cu in a submarine magmatic-hydrothermal system, Brothers volcano, Kermadec island arc. *Contributions to Mineralogy and Petrology* **173**, 1–16 (2018).
16. Knafelc, J., Bryan, S. E., Gust, D. & Cathey, H. E. Defining Pre-eruptive Conditions of the Havre 2012 Submarine Rhyolite Eruption Using Crystal Archives. *Front Earth Sci (Lausanne)* **8**, 549715 (2020).
17. Haase, K. M., Krumm, S., Regelous, M., Joachimski, M. & Isl, R. Oxygen isotope evidence for the formation of silicic Kermadec island arc and Havre – Lau backarc magmas by fractional crystallisation. *Earth Planet Sci Lett* **309**, 348–355 (2011).
18. Brophy, J. G. A study of rare earth element (REE)-SiO₂ variations in felsic liquids generated by basalt fractionation and amphibolite melting: A potential test for discriminating between the two different processes. *Contributions to Mineralogy and Petrology* **156**, 337–357 (2008).
19. Hirai, Y. *et al.* Magnesian Andesites from Kibblewhite Volcano in the Kermadec Arc, New Zealand. *Journal of Petrology* **64**, 1–23 (2023).
20. Hirai, Y. *et al.* Why are oceanic arc basalts Ca-rich and Ni-poor? Insights from olivine-hosted melt inclusions from Kibblewhite Volcano in the Kermadec arc. *Chem Geol* **662**, 122218 (2024).
21. Sugawara, T. Empirical relationships between temperature, pressure, and MgO content in olivine and pyroxene saturated liquid. *J Geophys Res Solid Earth* **105**, 8457–8472 (2000).

22. Wang, X. *et al.* A new clinopyroxene thermobarometer for mafic to intermediate magmatic systems. *European Journal of Mineralogy* **33**, 621–637 (2021).
23. Brey, G. P. & Köhler, T. Geothermobarometry in four-phase lherzolites II. new thermobarometers, and practical assessment of existing thermobarometers. *Journal of Petrology* **31**, 1353–1378 (1990).
24. Lepage, L. D. ILMAT: An Excel worksheet for ilmenite-magnetite geothermometry and geobarometry. *Comput Geosci* **29**, 673–678 (2003).
25. Putirka, K. Amphibole thermometers and barometers for igneous systems and some implications for eruption mechanisms of felsic magmas at arc volcanoes. *American Mineralogist* **101**, 841–858 (2016).
26. Waters, L. E. & Lange, R. A. An updated calibration of the plagioclase-liquid hygrometer-thermometer applicable to basalts through rhyolites. *American Mineralogist* **100**, 2172–2184 (2015).
27. Ridolfi, F. & Renzulli, A. Calcic amphiboles in calc-alkaline and alkaline magmas: Thermobarometric and chemometric empirical equations valid up to 1,130°C and 2.2 GPa. *Contributions to Mineralogy and Petrology* **163**, 877–895 (2012).
28. Mutch, E. J. F., Blundy, J. D., Tattitch, B. C., Cooper, F. J. & Brooker, R. A. An experimental study of amphibole stability in low-pressure granitic magmas and a revised Al-in-hornblende geobarometer. *Contributions to Mineralogy and Petrology* **171**, 1–27 (2016).
29. Spencer, K. J. & Lindsley, D. H. A solution model for coexisting Fe-Ti oxides. *American Mineralogist* **66**, 1189–1201 (1981).
30. Arató, R. & Audétat, A. FeTiMM - A new oxybarometer for mafic to felsic magmas. *Geochem Perspect Lett* **5**, 19–23 (2017).
31. Cabero, M. T., Mecoleta, S. & López-Moro, F. J. OPTIMASBA: A Microsoft Excel workbook to optimise the mass-balance modelling applied to magmatic differentiation processes and subsolidus overprints. *Comput Geosci* **42**, 206–211 (2012).
32. Ewart, A., Bryan, W. B., Chappell, B. W. & Rudnick, R. L. Regional geochemistry of the Lau-Tonga arc and backarc systems. *Proceedings of the Ocean Drilling Program, Scientific Results* **135**, 385–425 (1994).
33. Nandedkar, R. H., Hürlimann, N., Ulmer, P. & Müntener, O. Amphibole–melt trace element partitioning of fractionating calc-alkaline magmas in the lower crust: an experimental study. *Contributions to Mineralogy and Petrology* **171**, 1–25 (2016).

34. Nielsen, R. L., Gallahan, W. E. & Newberger, F. Experimentally determined mineral-melt partition coefficients for Sc, Y and REE for olivine, orthopyroxene, pigeonite, magnetite and ilmenite. *Contributions to Mineralogy and Petrology* **110**, 488–499 (1992).
35. Ghiorso, M. S. & Gualda, G. A. R. An H₂O–CO₂ mixed fluid saturation model compatible with rhyolite-MELTS. *Contributions to Mineralogy and Petrology* **169**, 1–30 (2015).
36. Ariskin, A. A. & Barmina, G. S. COMAGMAT: Development of a magma crystallization model and its petrological applications. *Geochemistry International* **42**, S1–S157 (2004).
37. Kelemen, P. B., Hanghøj, K. & Greene, A. R. One View of the Geochemistry of Subduction-Related Magmatic Arcs, with an Emphasis on Primitive Andesite and Lower Crust. in *Treatise on Geochemistry* vols 3–9 2–70 (Elsevier Inc., 2003).
38. Knafelc, J., Gust, D., Bryan, S. E., Anderson, M. & Cathey, H. E. Petrogenesis of Havre Volcano in the Kermadec Arc: 2012 Eruption of a Chemically Homogeneous Rhyolite. *Front Earth Sci (Lausanne)* **10**, 1 (2022).
39. Tamura, Y., Sato, T., Fujiwara, T., Kodaira, S. & Nichols, A. Advent of Continents: A New Hypothesis. *Sci Rep* **6**, 33517 (2016).
40. Miyashiro, A. Volcanic rock series in island arcs and active continental margins. *Am J Sci* **274**, 321–355 (1974).
41. Barsdell, M. & Berry, R. F. Origin and Evolution of Primitive Island Arc Ankaramites from Western Epi, Vanuatu. *Journal of Petrology* **31**, 747–777 (1990).
42. Timm, C. *et al.* Geochemical evolution of Monowai volcanic center: New insights into the northern Kermadec arc subduction system, SW Pacific. *Geochemistry, Geophysics, Geosystems* **12**, 1–20 (2012).
43. Taylor, R. N. *et al.* Mineralogy, chemistry, and genesis of the boninite series volcanics, Chichijima, Bonin Islands, Japan. *Journal of Petrology* **35**, 577–617 (1994).
44. Tamura, Y. & Tatsumi, Y. Remelting of an Andesitic Crust as a Possible Origin for Rhyolitic Magma in Oceanic Arcs: an Example from the Izu–Bonin Arc. *Journal of Petrology* **43**, 1029–1047 (2002).
45. Shukuno, H. *et al.* Origin of silicic magmas and the compositional gap at Sumisu submarine caldera, Izu-Bonin arc, Japan. *Journal of Volcanology and Geothermal Research* **156**, 187–216 (2006).

46. Tamura, Y. *et al.* Silicic magmas in the Izu-Bonin oceanic arc and implications for crustal evolution. *Journal of Petrology* **50**, 685–723 (2009).
47. Beard, J. S. & Lofgren, G. E. Dehydration melting and water-saturated melting of basaltic and andesitic greenstones and amphibolites at 1, 3, and 6.9 kb. *Journal of Petrology* **32**, 365–401 (1991).
48. Turner, S. *et al.* Magma evolution in the primitive, intra-oceanic Tonga arc: Rapid petrogenesis of dacites at Fonualei volcano. *Journal of Petrology* **53**, 1231–1253 (2012).
49. Storch, B., Regelous, M., Noebel, K. M., Haase, K. M. & Bauer, J. Extreme geochemical heterogeneity beneath the North Tonga Arc: Interaction of a subduction zone with intraplate seamount chains. *Chem Geol* **603**, 120903 (2022).
50. Pearce, J. A., Baker, P. E., Harvey, P. K. & Luff, I. W. Geochemical evidence for subduction fluxes, mantle melting and fractional crystallization beneath the south Sandwich island arc. *Journal of Petrology* **36**, 1073–1109 (1995).
51. Tamura, Y. *et al.* Mission Impossible: Distinct subduction components generate two primary magmas at Pagan Volcano, Mariana Arc. *Journal of Petrology* **55**, 63–101 (2014).
52. Gamble, J. A., Smith, I. E. M., McCulloch, M. T., Graham, I. J. & Kokelaar, B. P. The geochemistry and petrogenesis of basalts from the Taupo Volcanic Zone and Kermadec Island Arc, S.W. Pacific. *Journal of Volcanology and Geothermal Research* **54**, 265–290 (1993).
53. Gamble, J. A., Wright, I. C. & Baker, J. A. Seafloor geology and petrology in the oceanic to continental transition zone of the Kermadec-Havre-Taupo Volcanic Zone arc system, New Zealand. *New Zealand Journal of Geology and Geophysics* **36**, 417–435 (1993).
54. Gamble, J., Woodhead, J. O. N., Wright, I. A. N. & Smith, I. A. N. Basalt and Sediment Geochemistry and Magma Petrogenesis in a Transect from Oceanic Island Arc to Rifted Continental Margin Arc: the Kermadec-Hikurangi Margin, SW Pacific. *Journal of Petrology* **37**, 1529–1546 (1996).
55. Gamble, J. A., Christie, R. H. K., Wright, I. C. & Wysoczanski, R. J. Primitive K-rich magmas from Clark Volcano, southern Kermadec Arc; a paradox in the K-depth relationship. *The Canadian Mineralogist* **35**, 275–290 (1997).
56. Turner, S. *et al.* ^{238}U - ^{230}Th disequilibria, magma petrogenesis, and flux rates beneath the depleted Tonga-Kermadec island arc. *Geochim Cosmochim Acta* **61**, 4855–4884 (1997).

57. Haase, K. M., Worthington, T. J., Stoffers, P., Garbescho, D. & Wright, I. Mantle dynamics, element recycling, and magma genesis beneath the Kermadec Arc-Havre Trough. *Geochemistry Geophysics Geosystems* **3**, 1–22 (2002).
58. Wysoczanski, R. J. *et al.* The tectonomagmatic source of ore metals and volatile elements in the Southern Kermadec Arc. *Economic Geology* **107**, 1539–1556 (2012).
59. Timm, C. *et al.* Subduction of the oceanic Hikurangi Plateau and its impact on the Kermadec arc. *Nat Commun* **5**, 4923 (2014).
60. Timm, C. *et al.* Trench-perpendicular geochemical variation between two adjacent Kermadec arc volcanoes Rumble II East and West: The role of the subducted Hikurangi Plateau in element recycling in arc magmas. *Journal of Petrology* **57**, 1335–1360 (2016).
61. Umino, S. Magma mixing in boninite sequence of Chichijima, Bonin Islands. *Journal of Volcanology and Geothermal Research* **29**, 125–157 (1986).
62. Kanayama, K., Umino, S. & Ishizuka, O. Eocene volcanism during the incipient stage of Izu-Ogasawara Arc: Geology and petrology of the Mukojima Island Group, the Ogasawara Islands. *Island Arc* **21**, 288–316 (2012).

Figure captions

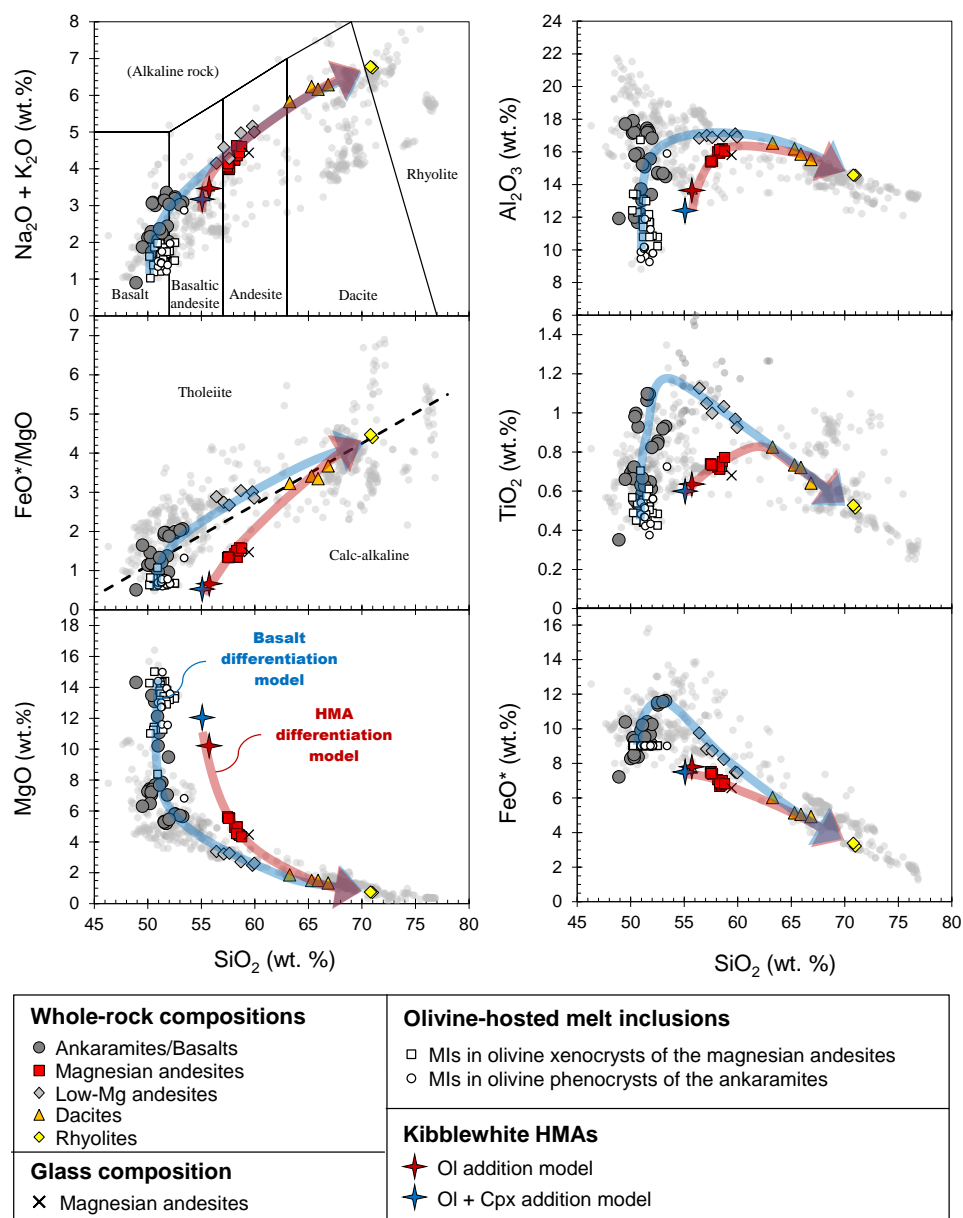


Figure 1. Major element variations in volcanic rocks from the Kibblewhite Volcano. Differentiation trends for primary andesites (Kibblewhite HMAs) and basalts (primitive basaltic melt inclusions: PBMI) are illustrated with red and blue arrows, respectively. Data points represent volcanic rocks and glasses from Kibblewhite Volcano¹⁹, while gray circles indicate published data from the Kermadec Arc^{9,13,14,32,52–60}. Open squares and circles show olivine-hosted melt inclusions from magnesian andesites and ankaramites²⁰. The discrimination boundary line in the FeO*/MgO-SiO₂ diagram follows Miyashiro⁴⁰.

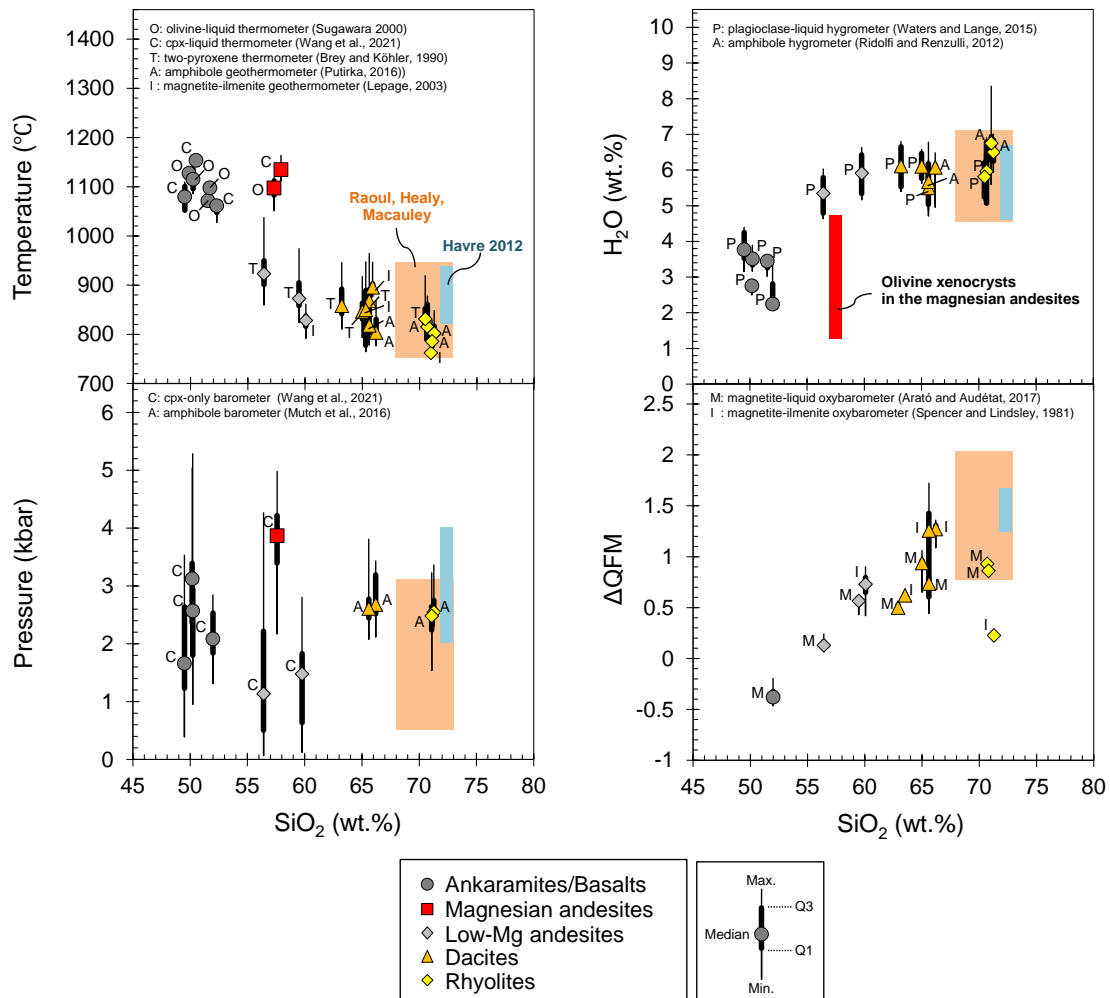


Figure 2. Calculated magmatic conditions (temperature, water content, pressure, and oxygen fugacity) for Kibblewhite magmas based on geothermobarometric analyses. The red shaded area highlights the estimated conditions for Kibblewhite HMAs¹⁹ while the orange and purple regions represent conditions for rhyolitic pumices from Raoul, Healy and Macauley¹⁴ and the 2012 Havre Volcano eruption¹⁶, respectively. The alphabetic labels near the data points denote the geothermobarometers used to determine these values (refer to the references within the graph).

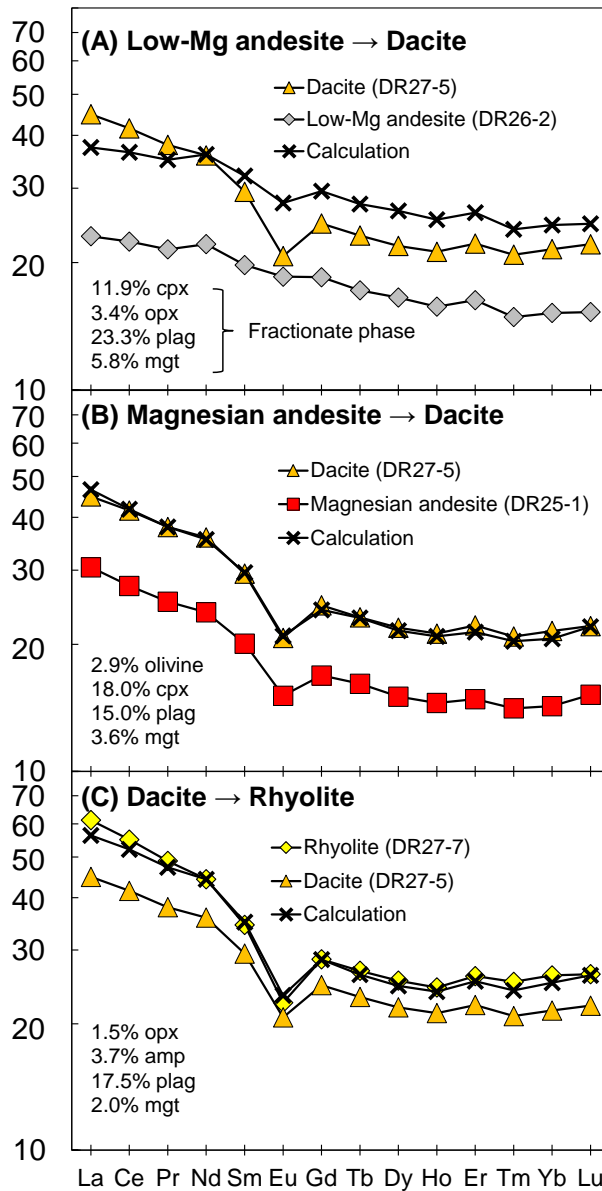


Figure 3. Rare-earth element (REE) patterns for observed and modeled daughter magmas in fractional crystallization models. Differentiation pathways include (A) low-Mg andesite to dacite, (B) magnesian andesite to dacite, and (C) dacite to rhyolite. Fractional crystallization of magnesian andesites better reproduces both major and REE compositions of dacites compared to low-Mg andesites. Calculated trends follow the Rayleigh fractionation model, with parameters listed in Tables S2.

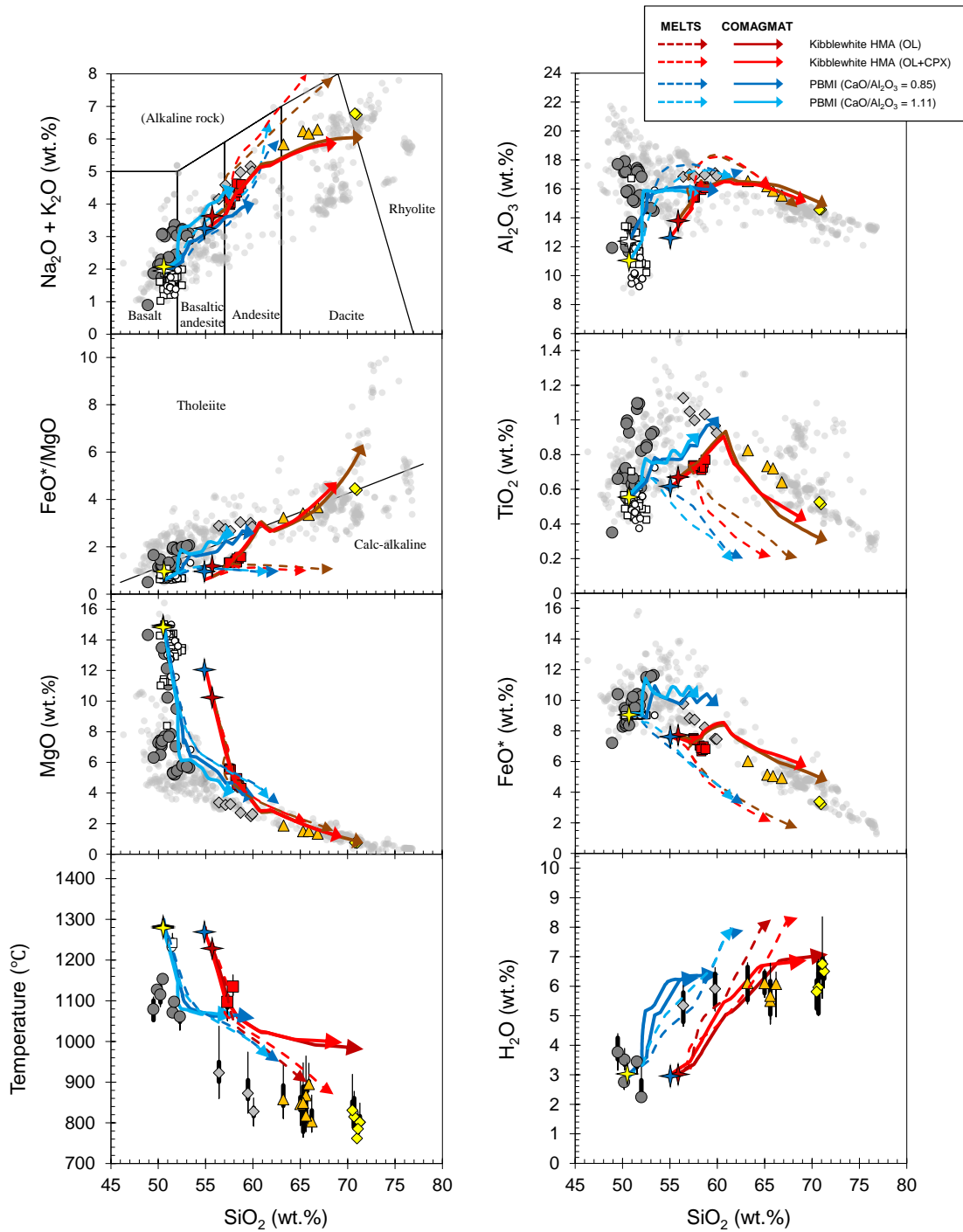


Figure 4. Thermodynamic fractional crystallization modeling of primary magmas using rhyolite-MELTS and COMAGMAT. Results show compositional changes during 70% crystal fractionation starting from Kibblewhite HMAs and PBMI. Andesitic primary magmas produce rhyolitic melts, while basaltic primary magmas yield andesitic compositions. The models assume an initial H₂O content of 3.0 wt.%, isobaric crystallization at 3 kbar, and an oxidation state constrained at $\Delta\text{QFM} + 1$.

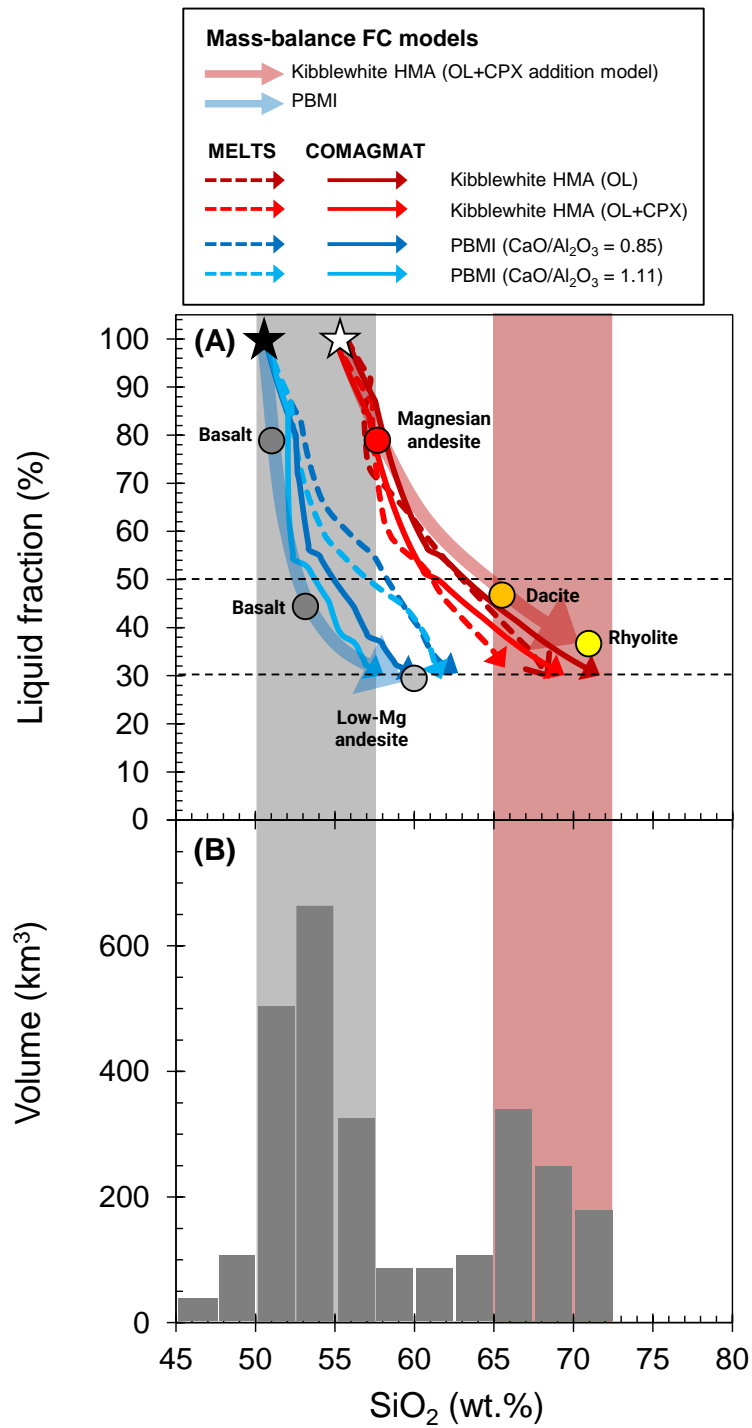


Figure 5. Bimodal distribution of SiO₂ contents in the Kermadec Arc. (A) SiO₂ versus remaining liquid fractions for the basalt and HMA differentiation models. Filled and open stars denote SiO₂ contents of PBMI and Kibblewhite HMAs, respectively. (B) Volume-weighted SiO₂ histogram of magmatic ejecta from Kermadec Arc⁹, showing peaks corresponding to fractional crystallization of primary basaltic and andesitic magmas.

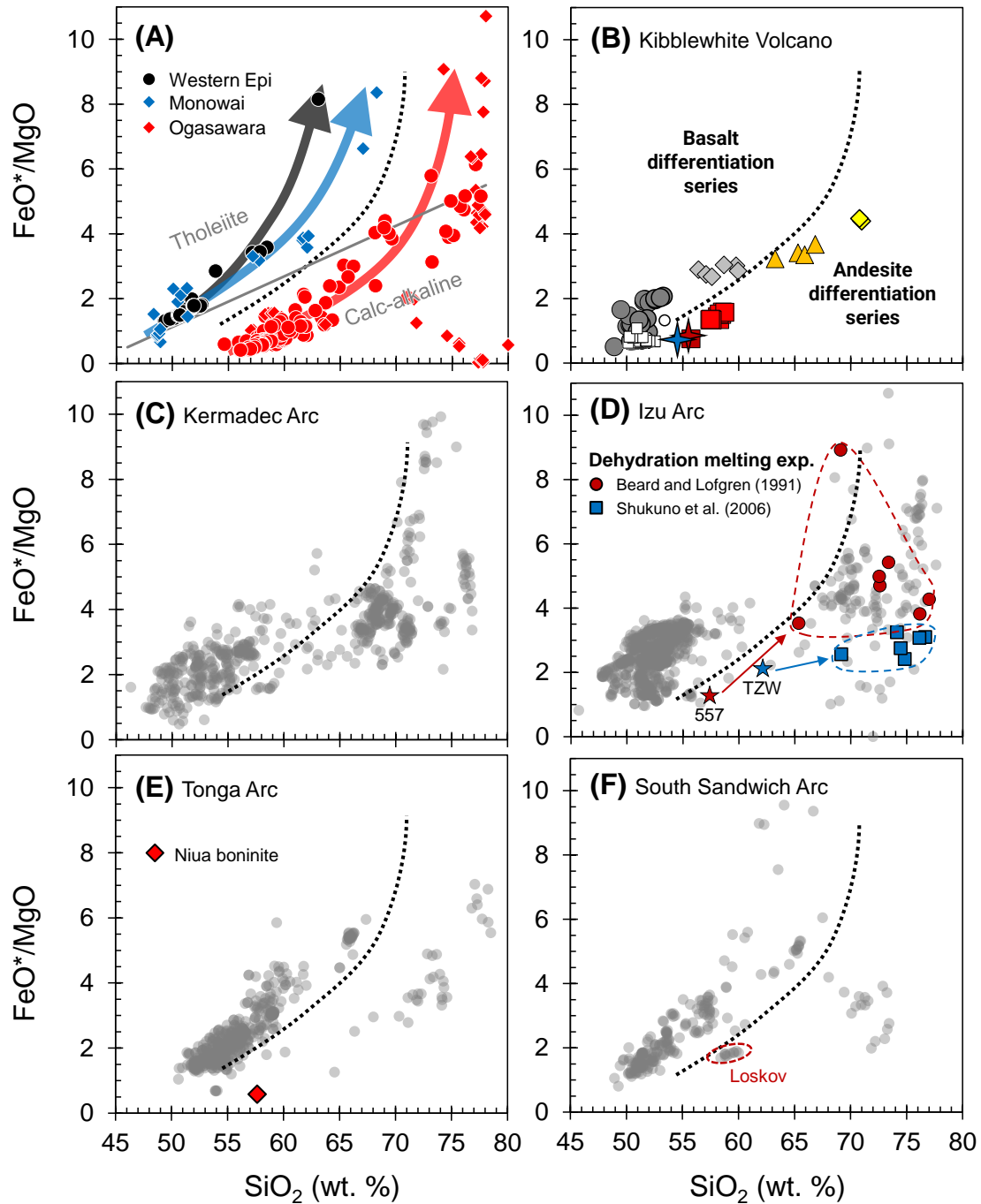


Figure 6. New FeO*/MgO–SiO₂ discrimination diagrams. (A) Comparison of differentiation trends for primary basaltic and andesitic magmas, highlighting limitations of the traditional Miyashiro⁴⁰ boundary (gray line) and introducing a new discrimination line (broken line). The new discrimination is applied to (B) Kibblewhite Volcano, (C) the Kermadec Arc, (D) the Izu Arc, (E) the Tonga Arc, and (F) the South Sandwich Arc. In (A), the black circles and blue diamonds represent the whole-rock compositions of Western Epi volcanic rocks in the Vanuatu Arc⁴¹ and the Monowai Volcanic Center in the Kermadec Arc⁴², respectively, while red circles and diamonds indicate whole-rock and glass compositions of boninites from the Ogasawara Islands in

the proto-Ogasawara Arc^{43,61,62}. The symbols and data sources in (B) and (C) are the same as that in Fig. 1. Volcanic rock data for the Izu Arc, Tonga Arc, and South Sandwich Arc were sourced from the GEOROC Database. In (D), red circles and blue squares represent the compositions of partial melts from dehydration melting experiments of magnesian andesite (sample 557)⁴⁷ and tonalite from the Tanzawa Plutonic Complex (TZM)⁴⁵, respectively. In (E), the red diamond indicates a boninite sample discovered at the Niua Volcanic Complex in the northernmost Tonga Arc⁴⁹.

Supplementary Materials

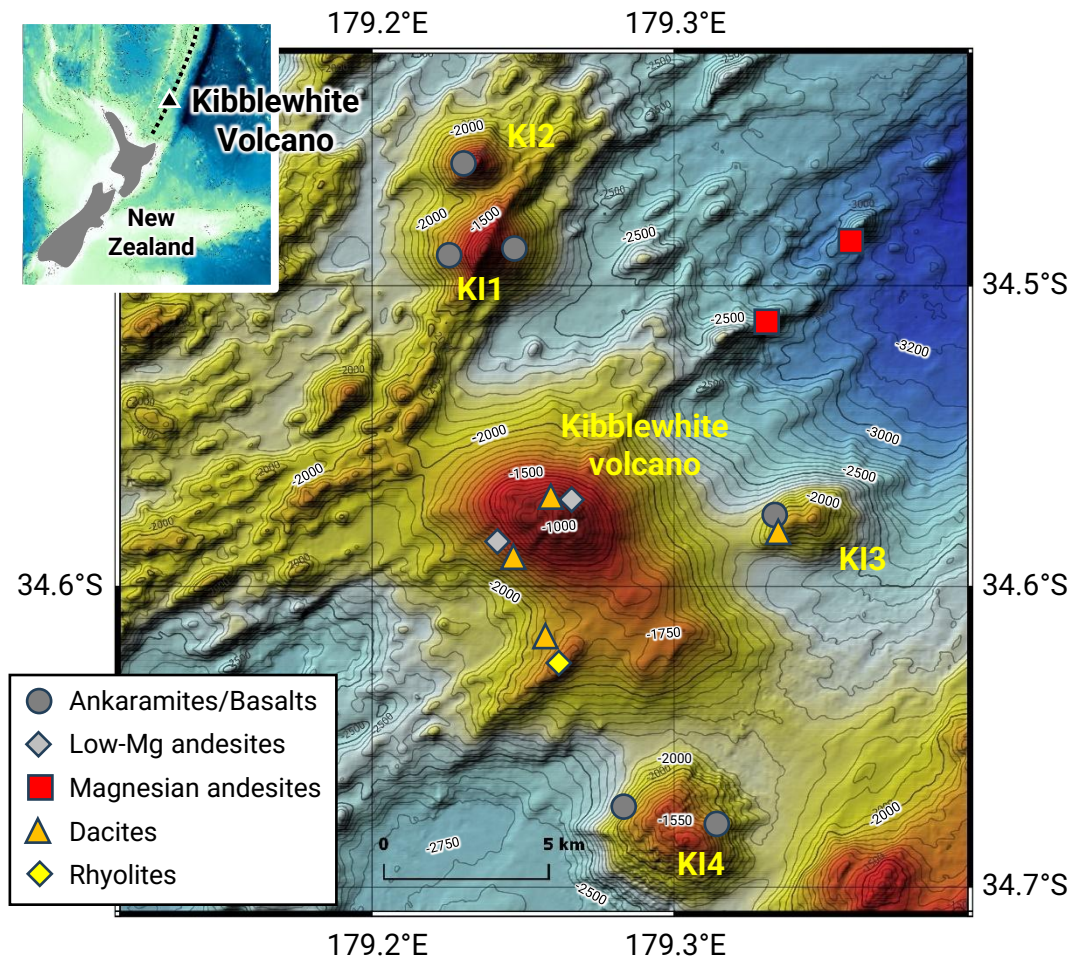


Figure S1. Bathymetric map of the Kibblewhite Volcano and the sample location. The markers indicate the magma types of the samples dredged from each location and correspond to the legend shown in Fig. 1. In the inset map, the volcanic front of the Kermadec Arc is depicted with black dashed lines, and the location of Kibblewhite Volcano is marked with a black triangle.

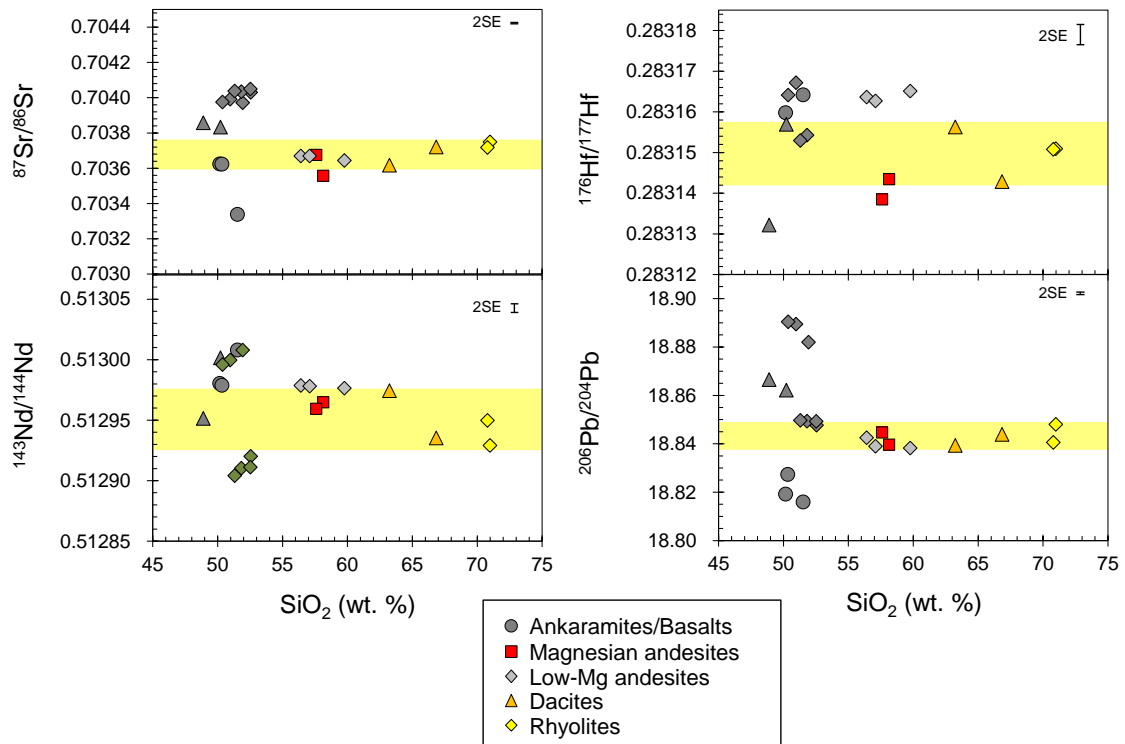


Figure S2. Relationship between SiO_2 content and Sr-Nd-Hf-Pb isotopic compositions in volcanic rocks from Kibblewhite Volcano. These isotopic ratios remain relatively constant during crystallization differentiation. Dacites and rhyolites are confined within the highlighted narrow limits, while low-Mg andesites and magnesian andesites fall within the indicated ranges. Data sourced from Hirai et al. (2023, 2024) and Hauff et al. (2021).

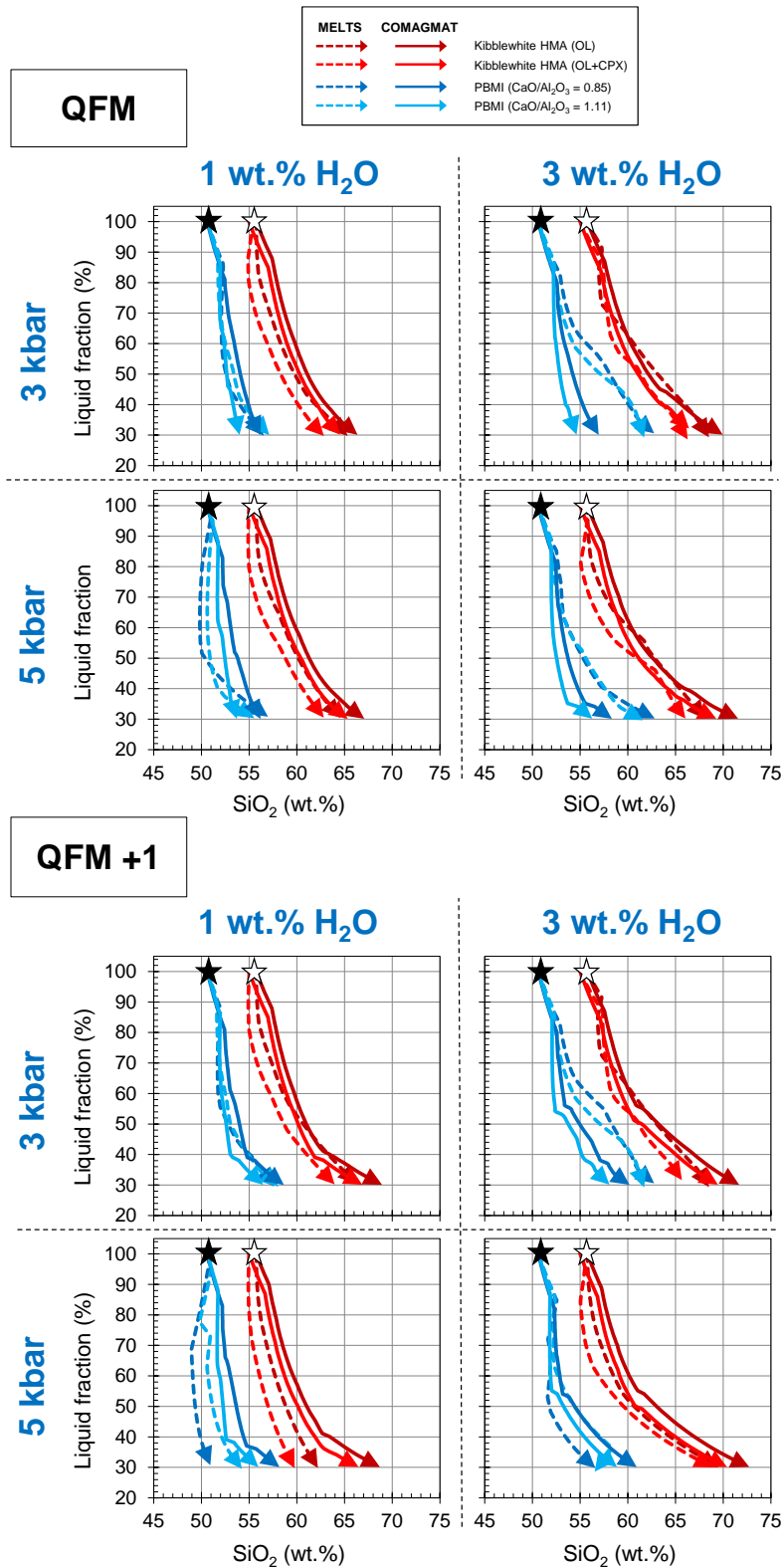


Figure S3. SiO₂ content versus residual liquid fraction for basaltic and high-magnesian andesite (HMA) differentiation models under varying initial magmatic conditions. Filled and open stars denote SiO₂ contents of PBMI and Kibblewhite HMAs, respectively.

Group	Sample	Method	Temperature (°C)					Pressure (kbar)		H ₂ O content (wt.%)		Oxidation state (ΔQFM)	
			Olivine-liquid	Cpx-liquid	Cpx-Opx	Magnetite-ilmenite	Amphibole composition	Cpx only	Al content in amphibole	Plagioclase-liquid	Amphibole	Magnetite-liquid	Magnetite-ilmenite
			Reference	Sugawara, 2000	Wang et al., 2021	Brey and Kohler, 1990	Spencer and Lindsley, 1985	Putirka, 2016	Wang et al., 2021	Mutch et al., 2016	Waters and Lange, 2015	Ridolfi and Renzulli, 2012	Arato and Audetat, 2017
Basalts	DR22-1	Q1	1127	1151			2.4		2.7				
		Q2	1127	1154			3.1		2.8				
		Q3	1128	1155			3.4		2.8				
		Min	1125	1149			1.9		2.5				
		Max	1133	1160			5.0		2.8				
Basalts	DR22-3	Q1	1071						3.3				
		Q2	1071						3.4				
		Q3	1075						3.5				
		Min	1070						3.0				
		Max	1079						3.5				
Basalts	DR29-1	Q1	1086	1048			1.8		2.2		-0.4		
		Q2	1098	1061			2.1		2.2		-0.4		
		Q3	1099	1064			2.5		2.8		-0.3		
		Min	1073	1028			1.3		2.1		-0.5		
		Max	1100	1068			2.8		3.5		-0.2		
Basalts	DR29-2	Q1	1096				1.8		3.3				
		Q2	1115				2.6		3.5				
		Q3	1135				2.9		3.6				
		Min	1096				1.0		3.2				
		Max	1144				5.3		3.9				
Basalts	DR29-23	Q1		1052			1.2		3.5				
		Q2		1079			1.7		3.8				
		Q3		1101			2.6		4.3				
		Min		1049			0.4		3.2				
		Max		1109			3.5		4.4				
Magnesian andesites	DR25-1	Q1	1083	1126			3.4						
		Q2	1097	1135			3.9						
		Q3	1112	1141			4.2						
		Min	1051	1113			2.2						
		Max	1119	1164			5.0						
Low-Mg andesites	DR26-1	Q1			858	816	0.6		5.3		0.5	0.6	
		Q2			873	828	1.5		5.9		0.6	0.7	
		Q3			905	837	1.8		6.4		0.6	0.8	
		Min			824	792	0.1		5.2		0.4	0.4	
		Max			974	861	2.8		6.6		0.6	0.9	
Low-Mg andesites	DR26-2	Q1			901		0.5		4.8		0.1		
		Q2			923		1.1		5.3		0.1		
		Q3			950		2.2		5.8		0.2		
		Min			860		0.1		4.6		0.1		
		Max			1037		4.3		6.0		0.2		
Dacites	DR26-16	Q1			838	888	795	2.5	5.0	5.9	0.7	1.2	
		Q2			868	895	804	2.7	5.5	6.1	0.7	1.3	
		Q3			891	902	831	3.2	6.2	6.1	0.8	1.3	
		Min			798	876	777	2.1	4.7	5.0	0.5	1.1	
		Max			964	946	868	3.4	6.3	6.5	0.9	1.4	
Dacites	DR27-5	Q1			831	777	803	2.4	5.8	5.4	0.9	0.6	
		Q2			846	850	818	2.6	6.1	5.7	0.9	1.3	
		Q3			863	889	837	2.8	6.5	6.2	1.0	1.4	
		Min			794	765	779	2.1	5.6	4.9	0.7	0.4	
		Max			918	947	892	3.8	6.6	6.8	1.1	1.7	
Dacites	DR27-9	Q1			842				5.5		0.5	0.6	
		Q2			858				6.1		0.5	0.6	
		Q3			892				6.7		0.5	0.6	
		Min			811				5.4		0.5	0.6	
		Max			946				6.8		0.5	0.6	
Rhyolites	DR27-1	Q1			794	760	795	2.5	5.1	6.3	0.9	0.2	
		Q2			815	762	802	2.5	6.0	6.5	0.9	0.2	
		Q3			861	764	817	2.8	6.8	6.8	0.9	0.2	
		Min			783	759	782	2.3	5.0	5.9	0.9	0.2	
		Max			877	765	848	3.4	6.9	7.0	1.0	0.2	
Dacites	DR27-7	Q1			814		776	2.2	5.2	6.3	0.8		
		Q2			831		786	2.5	5.8	6.8	0.9		
		Q3			852		799	2.6	6.2	6.9	0.9		
		Min			787		755	1.5	5.1	5.6	0.8		
		Max			919		828	3.2	6.5	8.4	0.9		

Table S1. Temperature, pressure, water content, and oxygen fugacity conditions of volcanic rocks from Kibblewhite Volcano estimated through the application of multiple geothermobarometers.

(a) PBMI (15 wt.% MgO) to Basalt MI (12 wt.% MgO)

	Parent	Daughter	Calculation	Fractionated phases		
	DR28-25_OL1_MI1 Melt inclusion	DR28-25_OL1_MI1 Melt inclusion		Oliv Fo89	Cpx Mg#90	Sp
Mass balance	100%		78.5%	5.6%	14.5%	1.4%
SiO2	50.44	50.88	51.03	40.52	54.91	0.07
TiO2	0.46	0.45	0.55	0.00	0.11	0.82
Al2O3	9.07	11.50	10.98	0.02	1.07	17.90
FeO	9.63	9.63	10.01	10.93	3.39	44.53
MnO	0.14	0.12	0.12	0.19	0.14	1.03
MgO	15.42	12.42	12.21	48.13	17.91	35.57
CaO	13.56	13.31	13.08	0.21	22.35	0.08
Na2O	1.03	1.38	1.28	0.00	0.13	0.00
K2O	0.25	0.31	0.32	0.00	0.00	0.00
		RSS	0.56			

(b) Basalt MI (12 wt.% MgO) to Basaltic andesite MI (7 wt.% MgO)

	Parent	Daughter	Calculation	Fractionated phases			
	DR28-25_OL1_MI1 Melt inclusion	DR28-25_OL5_MI2 Melt inclusion		Oliv Fo82	Cpx Mg#84	Plag An89	Sp
Mass balance	100%		59.4%	5.9%	29.6%	2.4%	2.7%
SiO2	50.88	53.17	53.18	39.23	53.14	46.57	0.08
TiO2	0.45	0.72	0.65	0.02	0.15	0.04	0.73
Al2O3	11.50	15.77	15.77	0.02	2.53	33.99	19.01
FeO	9.63	9.69	9.71	14.49	5.59	0.74	48.91
MnO	0.12	0.22	0.06	0.29	0.12	0.02	0.87
MgO	12.42	6.67	6.66	45.82	16.70	0.08	30.21
CaO	13.31	10.89	10.88	0.14	21.59	17.42	0.19
Na2O	1.38	2.34	2.18	0.00	0.18	1.14	0.00
K2O	0.31	0.51	0.52	0.00	0.00	0.00	0.00
		RSS	0.06				

(c) Basaltic andesite MI (7 wt.% MgO) to Low-Mg andesite

	Parent	Daughter	Calculation	Fractionated phases			
	DR28-25_OL5_MI2 Melt inclusion	DR26-2 Low-Mg andesite		Oliv Fo85	Cpx Mg#84	Plag An86	Mag
Mass balance	100%		65.7%	3.0%	16.8%	12.2%	2.4%
SiO2	53.17	56.52	56.53	39.23	53.61	47.26	0.21
TiO2	0.72	1.13	0.99	0.02	0.17	0.00	1.87
Al2O3	15.77	16.87	16.87	0.02	2.61	32.81	9.96
FeO	9.69	9.79	9.79	14.49	4.86	0.85	80.35
MnO	0.22	0.22	0.26	0.29	0.18	0.01	0.30
MgO	6.67	3.39	3.37	45.82	17.13	0.13	7.31
CaO	10.89	7.93	7.91	0.14	21.25	17.33	0.01
Na2O	2.34	3.35	3.21	0.00	0.19	1.60	0.00
K2O	0.51	0.81	0.78	0.00	0.00	0.00	0.00
		RSS	0.04				

Table S2. Results of least-squares fractional crystallization modelling.

(d) Low-Mg andesite to dacite

	Parent	Daughter	Calculation	Fractionated phase			
	DR26-2 Low-Mg andesite	DR27-5 Dacite		Cpx Mg#69	Opx Mg#62	Plag An66	Mag
Mass balance			55.6%	11.9%	3.4%	23.3%	5.8%
SiO ₂	56.52	65.43	65.45	50.42	53.59	51.56	0.12
TiO ₂	1.13	0.74	0.46	0.75	0.18	0.01	13.31
Al ₂ O ₃	16.87	16.22	16.20	4.55	1.31	30.33	2.41
FeO	9.79	5.15	5.20	11.33	20.16	0.53	81.39
MnO	0.22	0.14	0.18	0.40	0.82	0.01	0.65
MgO	3.39	1.51	1.42	14.32	22.34	0.05	2.09
CaO	7.93	4.58	4.58	17.92	1.60	13.66	0.03
Na ₂ O	3.35	4.47	4.34	0.32	0.02	3.77	0.00
K ₂ O	0.81	1.78	1.41	0.00	0.00	0.08	0.00
		RSS	0.24				

(e) Magnesian andesite to Dacite

	Parent	Daughter	Calculation	Fractionated phase			
	DR25-1 Magnesian andesite	DR27-5 Dacite		Oliv Fo85	Cpx Mg#85	Plag An86	Mag
Mass balance			60.8%	2.9%	18.0%	15.0%	3.4%
SiO ₂	57.68	65.43	65.44	39.23	53.55	47.26	0.11
TiO ₂	0.74	0.74	0.73	0.02	0.33	0.00	6.91
Al ₂ O ₃	15.46	16.22	16.22	0.02	2.59	32.81	6.05
FeO	7.46	5.15	5.15	14.49	5.64	0.85	82.29
MnO	0.15	0.14	0.18	0.29	0.12	0.01	0.33
MgO	5.57	1.51	1.50	45.82	17.59	0.13	4.31
CaO	8.96	4.58	4.55	0.14	19.98	17.33	0.00
Na ₂ O	2.86	4.47	4.24	0.00	0.20	1.60	0.00
K ₂ O	1.13	1.78	1.85	0.00	0.00	0.00	0.00
		RSS	0.06				

(f) Dacite to Rhyolite

	Parent	Daughter	Calculation	Fractionated phase			
	DR27-5 Dacite	DR27-7 Rhyolite		Amph Mg#67	Opx Mg#65	Plag An53	Mag
Mass balance			75.2%	3.7%	1.5%	17.5%	2.0%
SiO ₂	65.43	70.87	70.86	48.11	54.24	55.13	0.11
TiO ₂	0.74	0.53	0.59	1.82	0.06	0.00	10.93
Al ₂ O ₃	16.22	14.59	14.61	8.50	0.71	27.96	1.91
FeO	5.15	3.39	3.38	12.96	21.04	0.43	84.71
MnO	0.14	0.12	0.13	0.33	1.05	0.00	0.69
MgO	1.51	0.76	0.80	14.57	21.67	0.04	1.62
CaO	4.58	2.95	2.92	11.62	1.21	11.05	0.02
Na ₂ O	4.47	4.55	4.64	2.09	0.02	5.23	0.00
K ₂ O	1.78	2.24	2.33	0.00	0.00	0.16	0.00
		RSS	0.02				

Table S2. (continued)

HMA differentiation model	Kibblewhite HMA	→	Magnesian andesite	→	Dacite	→	Rhyolite				
Sample:			DR25-1		DR27-5		DR27-7				
SiO ₂	55.0		57.7		65.4		70.9				
MgO	12.1		5.6		1.5		0.8				
FeO*/MgO	0.6		1.3		3.4		4.5				
Remaining liquid fraction	1.00		0.79		0.48		0.36				
<i>Fractionation phase</i>											
Olivine		15%		2.9%		-					
Clinopyroxene		6%		18.0%		-					
Orthopyroxene		-		-		1.5%					
Hornblende		-		-		3.7%					
Plagioclase		-		15.0%		17.5%					
Spinel/Magnetite		-		3.4%		2.0%					
Total		21.0%		39.2%		24.8%					
Residual Sum of Squares (RSS)		-		0.06		0.02					
<hr/>											
Basalt differentiation model	Primitive basalt	→	Basalt	→	Basaltic andesite	→	Low-Mg andesite	→	Dacite	→	Rhyolite
Sample:	DR28-10 OL1_MI1		DR28-25 OL1_MI1		DR28-25 OL5_MI2		DR26-2		DR27-5		DR27-7
SiO ₂	50.4		50.9		53.2		59.9		65.4		70.9
MgO	15.4		12.4		6.7		2.5		1.5		0.8
FeO*/MgO	0.6		0.8		1.5		3.0		3.4		4.5
Remaining liquid fraction	1.00		0.79		0.47		0.30		0.17		0.13
<i>Fractionation phase</i>											
Olivine		5.6%		5.9%		3.0%		-			-
Clinopyroxene		14.5%		29.6%		16.8%		11.9%		-	-
Orthopyroxene		-		-		-		3.4%		1.5%	-
Hornblende		-		-		-		-		3.7%	-
Plagioclase		-		2.4%		12.2%		23.3%		17.5%	-
Spinel/Magnetite		1.4%		2.7%		2.4%		5.8%		2.0%	-
Total		21.5%		40.6%		34.3%		44.4%		24.8%	-
Residual Sum of Squares (RSS)		0.56		0.25		0.04		0.24		0.02	-

Table S3. Summary of mass balance fractional crystallization modelling for HMA and basalt differentiation models.

ID: Reference:	Kibblewhite HMAs		PBMI	
	OL addition Hirai et al. (2023)	OL-CPX addition Hirai et al. (2023)	DR25-3 OLB3-M1 Hirai et al. (2024)	DR25-3 OLP7-M1 Hirai et al. (2024)
SiO ₂ (wt.%)	55.8	55.0	50.6	51.2
TiO ₂	0.66	0.61	0.54	0.56
Al ₂ O ₃	13.7	12.6	12.3	10.8
FeO*	7.7	7.6	9.0	9.0
MnO	0.17	0.16	0.12	0.13
MgO	10.3	12.1	15.0	14.3
CaO	8.0	8.6	10.5	12.0
Na ₂ O	2.5	2.3	1.4	1.5
K ₂ O	1.00	0.90	0.45	0.50
P ₂ O ₅	0.13	0.12	0.07	0.10
Mg#	70.4	73.9	74.8	73.9
CaO/Al ₂ O ₃	0.58	0.68	0.85	1.11

Table S4. Initial melt compositions used for thermodynamic fractional crystallization modeling.